

Characterisation of Geological Samples with Dual-Energy XCT: A Comparison of Three Different Scanners

Margherita **Martini** (1, 6)* , Pierre **Francus** (1, 3) , Laurenz **Schröer** (4), Florian **Buyse** (4), Pierre **Kibleur** (4), Veerle **Cnudde** (4, 5), Leonardo **Di Schiavi Trota** (2) and Philippe **Després** (2)

(1) Centre Eau Terre Environnement, Institut national de la recherche scientifique, Québec, Canada

(2) Department of Physics, Physical Engineering and Optics, Université Laval, Québec, Canada

(3) GEOTOP – Research Centre on the Dynamics of the Earth System, Montréal, Québec H2X 3Y7, Canada

(4) Centre for X-ray Tomography (UGCT), Ghent University, Ghent, Belgium

(5) Department of Earth Science, Utrecht University, Utrecht, The Netherlands

(6) Present address: MatéIS, CNRS, UMR5510, Villeurbanne, France

* Corresponding author. e-mail: margherita.martini@inrs.ca and margherita.martini@insa-lyon.fr

The stoichiometric calibration method for dual-energy computed tomography (DECT) can be used in geosciences to characterise materials based on their effective atomic number (Z_{eff}) and their electron density (ρ_e) without previous knowledge of the incident X-ray beam. A stoichiometrically calibrated DECT method was applied here to measure these two properties on three different sedimentary rocks using three different X-ray CT instruments to determine which one is best to reveal the chemical composition or the mineralogical variations at the meso-scale. The three tested instruments: (1) a medical CT, (2) a custom-built micro-CT, and (3) a commercial micro-CT. Several acquisition settings were tested to identify the most suitable parameters for the characterisation the samples. Some parameters such as incident energies, resolution and calibration materials proved to have a significant impact on the accuracy of the characterisation. The determination of a general measurement protocol for geological samples was found to be difficult because of several complicating factors, including the nature of the sample, objectives of the study, and instrumental limitations that influence DECT characterisation. Nonetheless, comparison of the results obtained by the three scanners brings out the key parameters to be considered to perform a useful rock sample characterisation with DECT.

Keywords: computed tomography, characterisation, dual-energy, geology, scanners.

Received 14 Aug 24 – Accepted 26 Feb 25

X-ray Computed Tomography (CT) is an imaging technique used to visualise the external and inner structure of a sample in a non-destructive way. Even though it was originally developed for medical purposes, its potential in other fields became rapidly clear (Kalender 2011). The first non-medical application dates back to 1974, when Fourie (1974) studied the cranial morphology of an ancient tetrapod. Then, other research fields like archaeology (Re *et al.* 2015), biology (Mizutani and Suzuki 2012), marine science (Boesplug *et al.* 1995) and geology (Cnudde *et al.* 2006, Cnudde and Boone 2013) also utilised and benefited from CT scans. CT geological applications cover many topics, from the investigation of meteorites (Arnold *et al.* 1983), the study of igneous rocks (Baker *et al.* 2012), the analysis of sedimentary facies succession (Van Daele *et al.* 2014), to the reconstruction of the palaeoclimate through

varved lakes (Gagnon-Poiré *et al.* 2021). CT scans have also improved the pore structure characterisation (Dewankale *et al.* 2012, Blunt *et al.* 2013), useful for petroleum research, fluid flow experiments and for examining fractures in natural building stones (Vinegar and Wellington 1987, Keller 1997, Cnudde *et al.* 2011). Depending on the purpose of the research, the type of instrument may change, especially with respect to the required resolution and sample size; medical CT, micro-CT, nano-CT or synchrotron based CT could be used, even this research work will focus only on medical and lab-based micro-CT instrumentation (Boesplug *et al.* 1995, Akbari 2015, Ni *et al.* 2017, Zhao *et al.* 2018).

Materials of different composition may have similar X-ray attenuation using standard acquisition approaches, hence

doi: 10.1111/ggr.12608

© 2025 The Author(s). *Geostandards and Geoanalytical Research* published by John Wiley & Sons Ltd on behalf of International Association of Geoanalysts.

This is an open access article under the terms of the [Creative Commons Attribution License](https://creativecommons.org/licenses/by/4.0/), which permits use, distribution and reproduction in any medium, provided the original work is properly cited.

impeding a straightforward discrimination from CT images. Yet, advanced CT acquisition procedures have been developed further, e.g., phase-contrast imaging (Kastner *et al.* 2015), spectral (Godinho *et al.* 2021), dual-energy CT (Alves *et al.* 2015). Dual-energy CT (DECT) consists in imaging an object using two distinct tube voltages, a low and a high one, making use of the differential attenuation of the incident beams to facilitate the characterisation of two physical properties: the effective atomic number (Z_{eff} , related to chemical composition) and the electron density (ρ_{er} , generally proportional to the more common mass density). The main benefit of this methodology is the combination of non-destructive and three-dimensional materials characterisation. Moreover, it is easy to accomplish and not requires particular tools, as for example spectral CT. Here too, the DECT method was first developed for medical purposes, but geological applications quickly arose. Van Geet *et al.* (2000), adapting the mathematical formula of Coenen (1994), quantified for the first time the above-mentioned properties of reservoir rocks. Since then, many authors have used and improved DECT techniques to study geological materials (Duliu *et al.* 2003, Remeysen and Swennen 2008, Ilovea *et al.* 2009, Alves *et al.* 2015, Pazireh *et al.* 2016). One of the most recent DECT applications to Earth science is the work of Martini *et al.* (2021) and Martini *et al.* (2024). They applied a stoichiometric calibration method that previously had been developed to differentiate human tissues (Bourque *et al.* 2014) on minerals and varved sediment cores, respectively. Unlike the other DECT techniques, the stoichiometric calibration method has the significant advantage of not requiring the knowledge of the incident X-ray spectrum.

The present work aims to test the DECT methodology of Martini *et al.* (2021) on three different scanners (a medical CT, a custom-built micro-CT, and a commercial micro-CT) to compare the devices and to determine the best acquisition settings to characterise three rock samples of known composition. The paper discusses the best possible analytical procedure in the light of the wide range of settings tested (i.e., sets of calibration materials, multiple energies, different levels of resolution) using the three different instruments.

Materials and method

Samples: mineralogical and chemical analysis

Three different rock samples were analysed in this study: chalk from Dover, England, haematitic oolite from Clinton, NY, USA, and chert from Joplin, Missouri, USA (Figure 1).



Figure 1. Tested rock samples. Chalk (left), haematitic oolite (centre) and chert (right). The arrows indicate where test portions were extracted for destructive analyses.

About 20 mg of material were taken for destructive X-ray diffraction (XRD), inductively coupled plasma-atomic emission spectroscopy (ICP-AES) and carbon-hydrogen-nitrogen (CHN) measurements.

For XRD analyses, samples were first powdered and doped with corundum as per internal standard. Following this, the analyses were carried out using a PANalytical X'Pert Powder (Malvern PANalytical, Almelo, The Netherlands and Malvern, UK) at 45 kV and 40 mA at the Université du Québec à Rimouski. The XRD diffractograms were converted to mass fractions by *powdR* (Butler and Hillier 2021) and *Rocklock* (Eberl 2003) software, quantifying the main mineralogical components. The mass percentage of the total minerals calculated was normalised to 100%.

For the ICP-AES analyses, the samples were finely ground and subjected to alkaline fusion using lithium metaborate as the flux, with a flux-to-sample ratio of approximately 1 g of flux per 0.1 g of sample. They were analysed by an Agilent 5110 Dual View (Agilent Technologies, Mulgrave, Australia) at the Institut national de la recherche scientifique, Québec City. LKSD-2, LKSD-4, Buffalo and IAEA soil 7 were used for the verification of the calibration. The element mass fraction (mg kg^{-1}) is then converted to oxide percentages to represent how they occur in minerals.

CHN was performed using a Flash 2000 elemental analyser (Thermo Scientific, Waltham, USA) at the Institut national de la recherche scientifique, Québec City, obtaining the mass percentage of the three elements in relation to the analysed samples' mass (mg).

CT-scanners

Three X-ray CT devices were used. The first was a Somatom Definition AS+128 medical CT scanner (Siemens healthcare GmbH, Erlangen, Germany) located at the *Institut national de la recherche scientifique, Centre Eau Terre Environnement*, Canada. The X-ray tube could be operated between 70 kV and 140 kV at a current ranging between 20 mA and 800 mA, producing a fan beam. The instrument was equipped with an aluminium bowtie filter, aimed at reducing the dose for patients and cupping artefacts (Bushberg 2012); this filter also allowed the bandwidth of incident X-rays to be made smaller (Di Schiavi Trotta *et al.* 2022). The curved 64-row detector was from the StellarInfinity generation. The ADMIRE suite (statistical iterative reconstruction method) was used to reconstruct 512 × 512 pixel wide images. Voxels are anisotropic and the highest resolution was 0.1 × 0.1 × 0.6 mm (Gordic *et al.* 2014).

The second device was a HECTOR micro-CT system, located at Ghent University Centre for X-ray Tomography (UGCT), in Belgium. It was developed and built by UGCT (Masschaele *et al.* 2013). The X-ray tube could be operated up to 240 kV but was used at a maximum of 220 kV during the experiments, producing a cone beam. The X-ray tube could operate up to a maximum power of 280 W, while the minimum reachable focal spot size (at lower power) was 4 μm. A metal plate (e.g., Cu, Al or Sn) could be placed in front of the source to filter the beam. The 43 cm × 43 cm flat-panel detector (Varex) consisted of a caesium iodide scintillator, generating 2880 × 2880 pixel images. The image reconstructions were based on a Feldkamp-Davis-Kress (FDK) algorithm and were performed with the software *Octopus Reconstruction (XRE)* (Massenbroeck *et al.* 2006, 2007) developed in-house. Voxels are isotropic and the maximum achievable resolution was down to 4 μm (Masschaele *et al.* 2013).

A simulation software (*Arion*) developed at UGCT was also available to model sample attenuation when using the HECTOR scanner. Since *Arion* takes into account the incident spectrum specific to HECTOR, it provides very accurate image simulations (Dhaene *et al.* 2015). Indeed, the knowledge of the spectrum typically yields better results in dual-energy CT endeavours (Bourque *et al.* 2014), a hypothesis that was tested during this project. Because *Arion* is specific to HECTOR, simulations were limited to this device.

Finally, a CoreTOM micro-CT system (TESCAN, Brno – Kohoutovice, Czech Republic), located at the Institut national de la recherche scientifique, Centre Eau Terre Environnement,

Canada, was used as the third micro-CT device. It was developed and designed for multi-scale imaging; the X-ray tube operated between 30 kV and 230 kV, with a maximum power of 300 W, producing a cone beam. A metal plate (e.g., Cu, Al or Sn) could be placed in front of the source to filter the beam. The detector was a 42.8 cm × 42.8 cm flat panel (2856 × 2856 pixels), consisting of an amorphous Si and gadolinium oxysulfide scintillator. The TESCAN image reconstruction software *Panthera*, also based on the FDK algorithm, was used. Voxels are isotropic and the maximum resolution was approximately 3 μm (Van den Bulcke *et al.* 2019, Godinho *et al.* 2021). The CoreTOM system used is an upgraded and commercially available version of HECTOR. Since they hence have quite similar capabilities, it is of interest to see if similar measurements were produced in a DECT study.

DECT: Characterisation by stoichiometric method

The DECT method used here is identical to that described in Martini *et al.* (2021) and can be summarised as follows.

(a) The effective atomic number Z_{eff} and electron density ρ_e (number of electrons per unit volume, $e^- \text{ cm}^{-3}$) of a set of calibration materials having known composition were calculated using the following equations:

$$Z_{eff_Calc} = \beta \sqrt{\sum_i^N f_i Z_i^\beta} \quad (1)$$

$$\rho_{e_Calc} = \sum_{i=1}^N (Z_i/A_i) \rho \quad (2)$$

In Equation (1), f_i is the fractional mass of element Z_i . The exponent β is a function of photon energy, sample materials, instrument, and analytical specific settings (Landry *et al.* 2013, Alves *et al.* 2015, Azevedo *et al.* 2016) and can vary between 2.94 and 3.8 (Spiers 1946, Bonnin *et al.* 2014). In Equation (2), A_i is the atomic mass of the element Z_i and ρ is the material mass density (g cm^{-3}), calculated using a pycnometer (Manohara *et al.* 2008, Azevedo *et al.* 2016). In this paper, Z_{eff} and ρ_e obtained by Equations (1) and (2) are defined as “calculated” (Z_{eff_Calc} and ρ_{e_Calc}).

(b) The calibration samples were scanned and their attenuation coefficients for a given X-ray spectrum (low and high tube voltage, respectively μ_{low} and μ_{high}), were calculated from the attenuation grey values in the reconstructed images. The attenuation μ obtained from medical CT scanners is determined as follows given that Hounsfield

units (HU) are produced as output (Boespflug *et al.* 1995, Watanabe 1999):

$$\mu = \mu_{\text{sample}} / \mu_{\text{water}} = (\text{grey level expressed in HU units} / 1000) + 1 \quad (3)$$

For micro-CT the grey levels are not expressed in HU, instead they are determined by the slope and offset of the grey values histograms that are usually different for each sample, because they are based on the range of values chosen by the operator during the image reconstruction. Using the metadata of each image stack, the attenuation coefficient is calculated as follows:

$$\mu = (\text{grey level} * \text{slope}) + \text{offset} \quad (4)$$

The grey level histograms, and thus the attenuation coefficient histograms of natural rocks or minerals (Figure 2) are seldom normal because they often contain some degree of heterogeneity and thus their grey level histograms display some skewness. Therefore, to better capture this statistical particularity, both the mean and mode of grey values were tested as statistical descriptors of representative slices extracted in regions of interest (ROIs).

(c) The ratio of μ calculated from the calibration samples' scans obtained at low and high energy (Equations 3 or 4) are plotted against their calculated Z_{eff} (Equation 1), and a second-order polynomial empirical model is fitted to this data to obtain the Z_{eff} calibration equation.

$$Z_{\text{eff}} = a + b \cdot (\mu_{\text{low}} / \mu_{\text{high}}) + c \cdot (\mu_{\text{low}} / \mu_{\text{high}})^2 \quad (5)$$

(d) The ratio between measured μ (Equations 3 or 4) and calculated ρ_e (Equation 2) of calibration samples, normalised by the electron density of water ($\rho_{e \text{ water}} = 3.34 \text{ E}+23 \text{ e}^- \text{ cm}^{-3}$) and Z_{eff} determined in Equation (5) are plotted in a second step, again to obtain a second-order polynomial empirical model that can be used as a ρ_e calibration equation.

$$\mu_{\text{low or high}} / (\rho_e / \rho_{e \text{ water}}) = d + e \cdot Z_{\text{eff}} + f \cdot Z_{\text{eff}}^2 \quad (6)$$

In Equation (6), the μ values used can equally be those obtained at low or high energy. Once the two sets of calibration coefficients are found, Z_{eff} and ρ_e obtained by Equations (5) and (6) are then referred to as "measured" ($Z_{\text{eff.Meas}}$ and $\rho_{e.Meas}$).

All μ values were measured in a central zone of each rock sample to ensure a meaningful comparison with their mineralogical and chemical analyses.

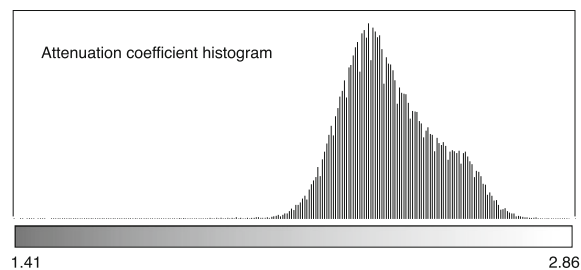


Figure 2. Example of a grey level histogram of a geological sample.

Data acquisition

As in Martini *et al.* (2021), calibration materials were scanned to determine the coefficients a to f of Equations (5) and (6), and this procedure was repeated for each instrument. Different sets of calibration materials (having a size comparable to the tested rock samples and stochastically chosen – see Table 1) were tested for the three scanners; calculated $Z_{\text{eff.Calc}}$ and $\rho_{e.Calc}$ values are presented in Table S1. Set b (Table 1) is the same as that used by Martini *et al.* (2021).

The rock samples were first scanned by medical-CT: the instrument, the acquisition parameters, the calibration materials (b -set) and the resulting coefficients a to f from Equations (5) and (6) are the same as those in Martini *et al.* (2021). However, some additional calculations were made: μ has been evaluated using not only the mode but also the mean of the grey level histogram, and $\rho_{e.Meas}$ has been measured using not only $\mu_{70 \text{ kV}}$ but also $\mu_{140 \text{ kV}}$. The scan time was about 5 s for both energies.

Before scanning the samples at UGCT with HECTOR, the in-house-developed software Arion (specifically, the set up

Table 1. Sets of calibration samples used for the tests

b-set	Same set of calibration materials of medical CT: NaI solutions at 50%, 40%, 30%, 25%, 20%, 15%, 10%, 8%, 5%, 1%, 0.5%, Al and Ti bar, halite, crystalline quartz, pyrite, fluorite and albite
r-set	Only solid materials: Al, Ti and Zn bar, crystalline quartz, albite, fluorite, halite, haematite, microcline and pyrite
y-set	Al, Ti and Zn bar, albite, crystalline quartz, fluorite, halite, microcline, pyrite, NaI solutions at 20%, 15%, 5% and 1%
c-set	Al, Ti and Zn bar, albite, crystalline quartz, fluorite, halite, haematite, microcline, NaI solutions at 20%, 15%, 5% and 1%
m-set	Al, Ti and Zn bar, albite, crystalline quartz, fluorite, halite, microcline, NaI solutions at 20%, 15% and 1%. This set of samples was also tested using the Hector scanner.
g-set	Al, Ti and Zn bar, albite, crystalline quartz, fluorite, halite, microcline, NaI solutions at 20%, 15%, 5% and 1%

optimiser module) (Dhaene *et al.* 2015), simulating the detector spectral sensitivity and the related linear attenuation coefficient of samples, was used to test numerous scanner settings, and find the ones that would allow the best sample characterisation. Considering the size and density of investigated samples, some parameters were fixed: power at 25 W, isotropic voxel size set at 25 μm , 1 mm Cu plate filter. The simulations of the μ of the three rock samples as measured by the HECTOR scanner used the following tube voltages: 90, 110, 120, 130, 140, 160, 170 and 220 kV. These linear attenuation coefficients were then used to obtain simulated $Z_{\text{eff_Meas}}$ and $\rho_{\text{e_Meas}}$ ($Z_{\text{eff_Meas_Sim}}$ and $\rho_{\text{e_Meas_Sim}}$).

The samples were then scanned with the HECTOR instrument using the best settings found in the simulations, which were 110 and 220 keV, 25 W, 1 mm Cu filter, reaching a resolution of 25 μm . About 1200 projections were acquired, mean 1 and binning 2 \times 2. The exposure time changed depending on the used energy to prevent saturating the detector. The acquisition duration for each sample ranged from 15 to 20 min for the scans taken at 220 kV and 1 h for the scans taken at 110 kV.

In the third part of the project, the samples were scanned with the CoreTOM device. Two different acquisition conditions were chosen: one aiming to emulate the HECTOR scanner, thus using the same settings, and another that covered a wider energy range. For the second setting, a 1.5 mm Cu plate was placed in front of the X-ray source to filter out the lower energy components. Then, all the samples were scanned at 90, 160 and 230 kV offering three energy ratios (90/160, 90/230, 160/230). CoreTOM was operated at a power of 50 W, and the reconstructed voxel size was set to 50 μm . About 1000 projections have been acquired (mean 1 and binning 2 \times 2). Again, the exposure time was changed depending on the used voltage to avoid the detector saturation. Here, all the calibration sets listed in Table 1 were tested to find the one which best characterised the three rock samples. The acquisition duration for each sample was about 15 min for the scans taken at 90 kV, about 45 min for the scans taken at 160 kV, and about 1 h for the scans taken at 230 kV.

Results

XRD, ICP-AES and CHN

The XRD results indicating the mineralogy of the three rock samples are shown in Table 2. The elemental mass

Table 2.
Mineralogical composition (expressed as percentages) of the three rock samples measured by XRD

Identified minerals (by XRD)	Chalk	Haematitic oolite	Chert
Quartz	13.1%	14.7%	100.0%
K feldspar	0.5%	0.4%	-
Calcite	85.9%	-	-
Fe-dolomite	-	30.3%	-
Diopside	-	0.7%	-
Fosterite	-	1.3%	-
Pyrite	-	0.2%	-
Haematite	-	35.0%	-
Fluorapatite	-	3.1%	-
Kaolinite	-	1.5%	-
Chlorite	-	13%	-
Illite	0.5%	-	-
Total	100%	100%	100%

Table 3.
Element mass fraction determined by ICP-AES and CHN analysis in chalk, haematitic oolite and chert

Detected elements	% in Chalk	% in Haematitic oolite	% in Chert
Al	0.82%	2.01%	*
Ca	30.23%	7.65%	0.1%
Fe	0.81%	30.99%	0.3%
K	0.38%	*	*
Mg	0.3%	3.18%	*
Mn	*	0.27%	-
Na	*	*	0.02%
P	0.18%	0.41%	-
Si	7.67%	7.57%	45.81%
S	*	0.39%	*
Ti	0.11%	*	-
As, Ba, Cd, Co, Cr, Cu, La, Mo, Ni, Pb, Sc, Sr, V, Y, Zn, Zr	*	*	*
C	9.45%	4.4%	0%
H	-	-	-
O	49.78%	42.83%	53.61%
Total	100%	100%	100%

* Mass fraction < 0.1%.

fraction of the rock specimens was determined by both ICP-AES and CHN and these, outlined in Table 3, allowed to precisely calculate $Z_{\text{eff_Calc}}$ using Equation (1) and $\rho_{\text{e_Calc}}$ using Equation (2) (Table 4).

Medical-CT experiments

Calibration curves for the medical CT scanner are illustrated in Figure 3. The μ values at low and high tube voltage of the three samples were determined using Equation (3). Their measured $Z_{\text{eff_Meas}}$ and $\rho_{\text{e_Meas}}$ were obtained using Equations (5) and (6) and calculated for

Table 4.
Calculated $Z_{\text{eff_Calc}}$ and $\rho_{\text{e_Calc}}$ values of chalk, haematitic oolite and chert

Rock	$Z_{\text{eff_Calc}}$	$\rho_{\text{e_Calc}}$
Chalk	14.67	4.35E+23
Haematitic oolite	18.81	7.70E+23
Chert	11.75	7.00E+23

The electron density ρ_{e} values are in units of moles $\text{e}^- \text{cm}^{-3}$.

both mean and mode of the grey level histogram. The two calibration curves already obtained by Martini *et al.* (2021) are reported in Figure 3d (Z_{eff} model using the mode of grey level histogram in μ calculation) and (e) (ρ_{e} model using $\mu_{70 \text{ kV}}$ and the mode of grey level histogram in μ calculation) in Figure 3. The correlation coefficients for the calibration curves are quite similar (between 0.96 and 0.98). All curves are convex. The 8% NaI is an outlier in Figure 3b, c, e and f, while Ti is an outlier in (a) and (d).

Table 5 presents the difference between the calculated $Z_{\text{eff_Calc}}$ and $\rho_{\text{e_Calc}}$ (Table 4) and the measured ones with dual-energy medical CT. Differences range from 0.04% for chalk's $Z_{\text{eff_Calc}}$ using the attenuation's histogram mean, to 21.4% for chalk's $\rho_{\text{e_Meas}}$ using $\mu_{70 \text{ kV}}$ and attenuation's histogram mode.

Arion and HECTOR experiments

Twenty-eight acquisition settings (different low energies and different sets of calibration materials) were tested with Arion: the calibration curves were plotted using linear attenuation coefficients obtained from the software. Simulated calibration curves obtained with *m*-set of reference materials and 110 kV as low energy are illustrated in Figure 4. The correlation coefficients R^2 are above 0.96 in all cases.

Table 6 shows $Z_{\text{eff_Meas_Sim}}$ and $\rho_{\text{e_Meas_Sim}}$ values (from Arion simulations) determined using Equations (5) and (6) and the percentage difference with the calculated properties ($Z_{\text{eff_Calc}}$ and $\rho_{\text{e_Calc}}$ Table 4).

The results obtained using the *m*-set and the ratio $\mu_{110 \text{ kV}} / \mu_{220 \text{ kV}}$ are the closest to calculated values for all three rocks and range between 0.3% and 23.8%, with 8 out of 9 being $> 14\%$. The outcomes from the other sets of calibration materials are presented in Table S2.

The best acquisition parameters determined by the Arion (module Optimizer) were used to scan the three samples with the HECTOR scanner at 110 kV and 220 kV. Six

calibration curves (Figure 5) were obtained using the *m*-set of calibration materials (Table 1). They have the same shape as those obtained with Arion, but with lower R^2 , ranging from 0.91 to 0.94.

The rock samples μ values at both energies were obtained using Equation (4), and their $Z_{\text{eff_Meas}}$ and $\rho_{\text{e_Meas}}$ values were retrieved using Equations (5) and (6). For each evaluation both mean and mode of grey level histogram were used. Table 7 presents the difference between the calculated 304 $Z_{\text{eff_Calc}}$ and $\rho_{\text{e_Calc}}$ (Table 4) and the values measured with the HECTOR scanner. They range 305 between 0.05% and 8.5% with fifteen values out of eighteen less than or equal to 4%.

CoreTOM experiments

The same acquisition conditions used for experiments with the HECTOR scanner and the same set of calibration materials (*m*-set) were used for the CoreTOM scanner. Figure 6 shows the calibration curves obtained using the mean of grey level histogram to calculate μ (a is Z_{eff} model, b ρ_{e} model using $\mu_{110 \text{ kV}}$ and c ρ_{e} model using $\mu_{220 \text{ kV}}$) and the mode (d is Z_{eff} model, e ρ_{e} model using $\mu_{110 \text{ kV}}$ and f ρ_{e} model using $\mu_{220 \text{ kV}}$). They all have a convex shape and with R^2 values of 0.88 and 0.97.

Table 8 presents the results obtained with CoreTOM using the same settings as those of Table 7 for HECTOR: μ values at both energies were calculated using Equation (4), and their $Z_{\text{eff_Meas}}$ and $\rho_{\text{e_Meas}}$ values were measured using Equations (5) and (6) with both mean and mode of the grey level histogram. Differences between the calculated $Z_{\text{eff_Calc}}$ and $\rho_{\text{e_Calc}}$ and the measured ones vary between 0.7% and 22.7%.

Different calibration settings aiming to investigate a wider range of energies and calibration sets were performed: Figure 7 shows the curves for Z_{eff} and ρ_{e} models obtained using the *g*-set of calibration materials (Table 1). Three different energies couples (90/160, 90/230 and 160/230 kV) were used. The correlation coefficients are between 0.85 and 0.96, lower values than those previously obtained using the settings similar to HECTOR. Once more, they are quite similar when the mean and the mode are compared. ρ_{e} models obtained with $\mu_{230 \text{ kV}}$ (both mean and mode of the grey levels, Figure 7f, l) had the highest R^2 values. Z_{eff} calibration curves change shape depending on the energy used, while ρ_{e} calibration curves do not. The calibration curves for the other calibration sets are available in online supporting information Figures S1A and S1B.

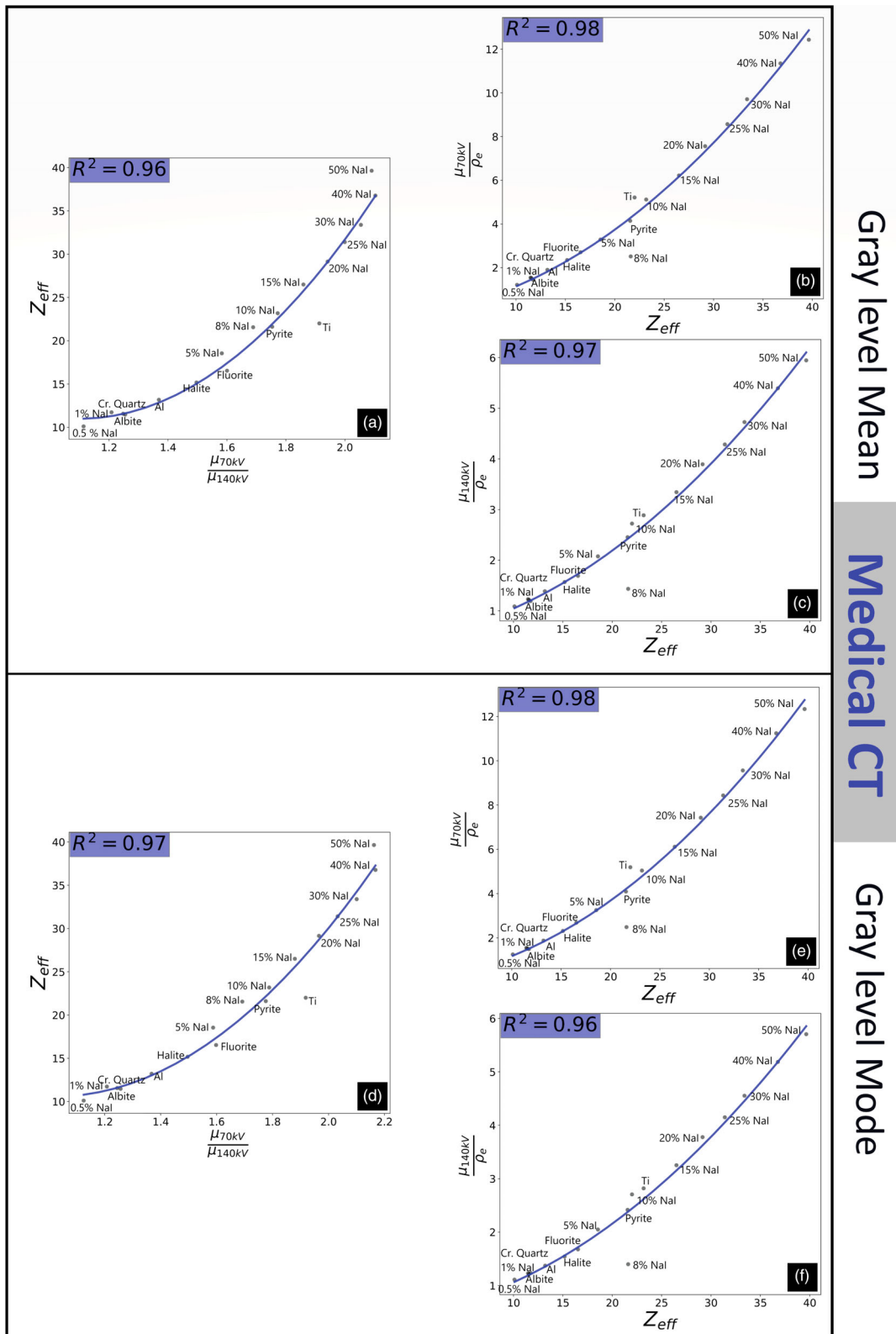


Figure 3. Calibration curves determined with the medical CT scanner using the *b*-set of calibration samples. Using the mean of grey level histogram, there is (a) Z_{eff} model; (b) ρ_e model using $\mu_{70\text{ kV}}$; (c) ρ_e model using $\mu_{70\text{ kV}}$. Using the mode of grey level histogram, there is (d) Z_{eff} model; (e) ρ_e model using $\mu_{70\text{ kV}}$; (f) ρ_e model using $\mu_{70\text{ kV}}$. (d) and (e) are identical to the calibration curves of Martini *et al.* (2021).

Table 5.

$Z_{eff.Meas}$ and $\rho_{e.Meas}$ of the three rock samples measured using DECT and using both mean and mode of grey level histograms obtained with the medical CT scanner

	Medical CT			
	Chalk	Haematitic oolite	Chert	
$Z_{eff.Calc}$	14.67	18.81	11.75	
$\rho_{e.Calc}$	4.35E+23	7.70E+23	7.00E+23	
$Z_{eff.Meas}$	14.63	20.67	11.59	Grey level Mode
% difference	0.3%	9.9%	1.3%	
$\rho_{e.Meas}$ using $\mu_{70 kV}$	5.29E+23	7.97E+23	7.71E+23	
% difference	21.4%	3.5%	10.1%	
$\rho_{e.Meas}$ using $\mu_{140 kV}$	5.15E+23	7.96E+23	7.60E+23	
% difference	18.3%	3.3%	8.6%	
$Z_{eff.Meas}$	14.66	16.46	11.47	Grey level Mean
% difference	0.04%	12.5%	2.4%	
$\rho_{e.Meas}$ using $\mu_{70 kV}$	4.78E+23	8.98E+23	7.62E+23	
% difference	9.9%	16.7%	8.8%	
$\rho_{e.Meas}$ using $\mu_{140 kV}$	4.64E+23	8.84E+23	7.46E+23	
% difference	6.8%	14.8%	6.6%	

The percentage difference is with the calculated properties $Z_{eff.Calc}$ and $\rho_{e.Calc}$ of Table 4. The electron density ρ_e values are in units of moles $e^- cm^{-3}$.

Table 9 reports for the CoreTOM scanner the $Z_{eff.Meas}$ and $\rho_{e.Meas}$ values obtained using Equations (5) and (6), as well as the differences between the calculated $Z_{eff.Calc}$ and $\rho_{e.Calc}$. The latter oscillate between 0.002 and 30.4%. Measurement results for other sets of calibration material are available in Tables S3A and S3B.

Discussion

XRD analysis (Table 2) showed that the chalk and haematitic oolite samples are mineralogically heterogeneous, whereas the chert is only made of quartz. μ -CT slices of these rocks (Figure 8) illustrate that chalk (left) and chert (right) have a homogeneous dense texture, but the haematitic oolite (centre) is very heterogeneous at this resolution. Note that for the haematitic oolite only an oolitic section was selected, where parts rich in haematite are brighter, while the rest corresponds to a more silicate component. Characterising this rock samples with DECT was challenging since the analysed samples in previous work had simpler chemical composition and less mineralogical variability (Remeysen and Swennen 2008, Alves *et al.* 2015).

The stoichiometric calibration method, designed for a medical-CT instrument and medical purposes, was applied here for the very first time to a micro-CT in geological studies. Although other authors have used dual-energy methods to

characterise geological materials, the stoichiometric calibration method stands out for its simplicity. For instance, the work of Pazireh *et al.* (2016) is noteworthy, but they have assumed knowledge of the spectra, making the workflow more difficult.

Medical CT

The calibration curves reported in Figure 3 yielded high correlation coefficients. There is no significant difference between the curves obtained with the mean or the mode of grey level values. One outlier is present in each curve, but, as reported previously by Martini *et al.* (2021), it is difficult to explain why they appear because they are values for NaI solution samples that otherwise perform very well. Despite these outliers the calibration is efficient, as already reported by Martini *et al.* (2021) who successfully identified several pure common minerals using this DECT protocol and this medical scanner. They obtained a difference for both properties (Z_{eff} and ρ_e) of about 2% for a pure calcite and about 1% for quartz, slightly lower than values reported here for rock samples (Table 5, grey level mode). However, their pure haematite was characterised by a difference of 22% for Z_{eff} and 14% for ρ_e which is larger than the value obtained for the haematitic oolite (about 10% for Z_{eff} and 4% for ρ_e Table 5, grey level mode). To understand these differences, some factors should be considered. Martini *et al.* (2021) compared their measured Z_{eff} and ρ_e with theoretical properties of commercially purchased reference minerals with no control on the possibility of the materials containing impurities. The samples here are natural rocks and not reference materials, so porosity (thus, density) and heterogeneity have an influence on the X-ray attenuation. For example, the theoretical electron density of haematite was estimated to be about $1.5E+24 e^- cm^{-3}$ in Martini *et al.* (2021), whereas it is only $7.7E+23 e^- cm^{-3}$ (Table 4) for the haematitic oolite analysed here: a lower density entails a better signal-to-noise ratio (especially at 70 kV) and in turn a better material discrimination (Hendee 2002).

In this experiment, the effect of choosing between mean and mode for μ calculation was tested. For the medical CT scanner, the determined μ values were not significantly different. However, among the results presented in Table 5, one is noteworthy: the percent difference between measured and calculated properties of haematitic oolite was always smaller when the mode of the grey level histogram was used. Tables 2 and 3 show that the rock is heterogeneous, and Figure 9 that its μ distribution skewed towards the lower values. Therefore, using the mode seems more suitable to characterise such heterogeneous samples.

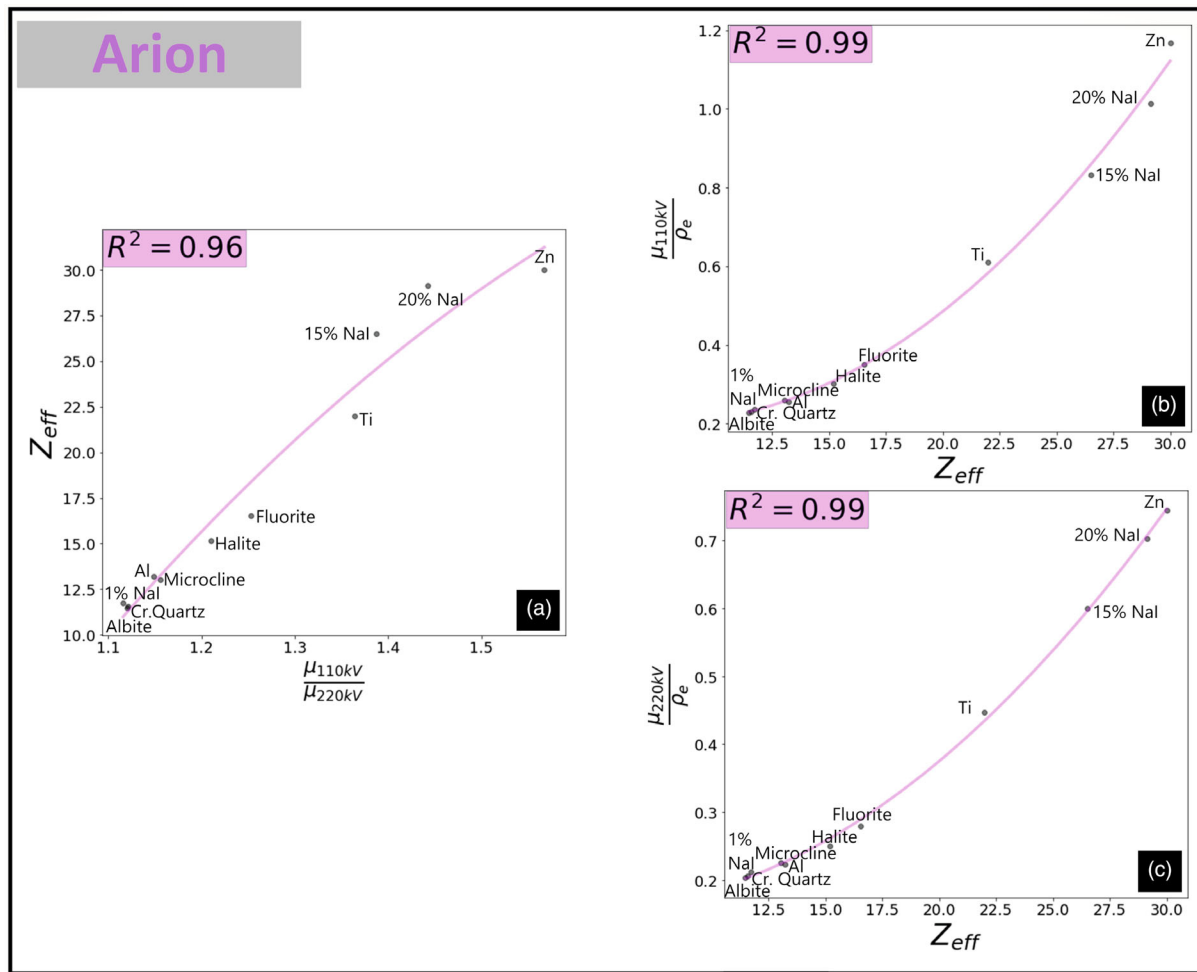


Figure 4. Arion calibration curves. (a) Z_{eff} calibration using simulated $\mu_{110\text{ kV}}/\mu_{220\text{ kV}}$ (b) ρ_e calibration using simulated $\mu_{110\text{ kV}}$ (c) ρ_e calibration using simulated $\mu_{220\text{ kV}}$. Note that a mean and a mode cannot be extracted for the μ values simulated by the Arion Optimizer.

Table 6. Properties of the studied rocks using the μ simulated values with the Arion Optimizer ($Z_{eff_Meas_Sim}$ and $\rho_{e_Meas_Sim}$) and the percentage difference with calculated properties (Z_{eff_Calc} and ρ_{e_Calc} of Table 4)

	Arion		
	Chalk	Haematitic oolite	Chert
Z_{eff_Calc}	14.67	18.81	11.75
ρ_{e_Calc}	4.35E+23	7.70E+23	7.00E+23
$Z_{eff_Meas_Sim}$	16.72	23.33	11.71
% difference	14%	24.05%	0.3%
$\rho_{e_Meas_Sim}$ using $\mu_{110\text{ kV}}$	5.12E+23	5.87E+23	5.93E+23
% difference	17.7%	23.8%	15.3%
$\rho_{e_Meas_Sim}$ using $\mu_{220\text{ kV}}$	5.04E+23	5.88E+23	5.93E+23
% difference	15.9%	23.7%	15.3%

The electron density ρ_e values are in units of moles $e^- \text{ cm}^{-3}$.

Another important consideration about the outcomes obtained by Martini *et al.* (2021) is that they opted for μ_{low} in the ρ_e model because the correlation was stronger. Indeed, Figure 3 shows $R^2 = 0.98$ in the ρ_e model using $\mu_{70\text{ kV}}$ and $R^2 = 0.96$ in the ρ_e model using $\mu_{140\text{ kV}}$. However, as described in Table 5, this is not always true: haematitic oolite presents an electron density that is closer to the calculated value using $\mu_{140\text{ kV}}$ probably because of the higher X-ray penetration.

Arion and HECTOR

The calibration curves obtained using the μ values from Set-up Optimizer (Figure 4) yielded the highest correlation coefficients (i.e., R^2 between 0.96 and 0.99), although the Z_{eff} calibration curves do not perfectly fit all the data points. This mismatch between curves and data points is more

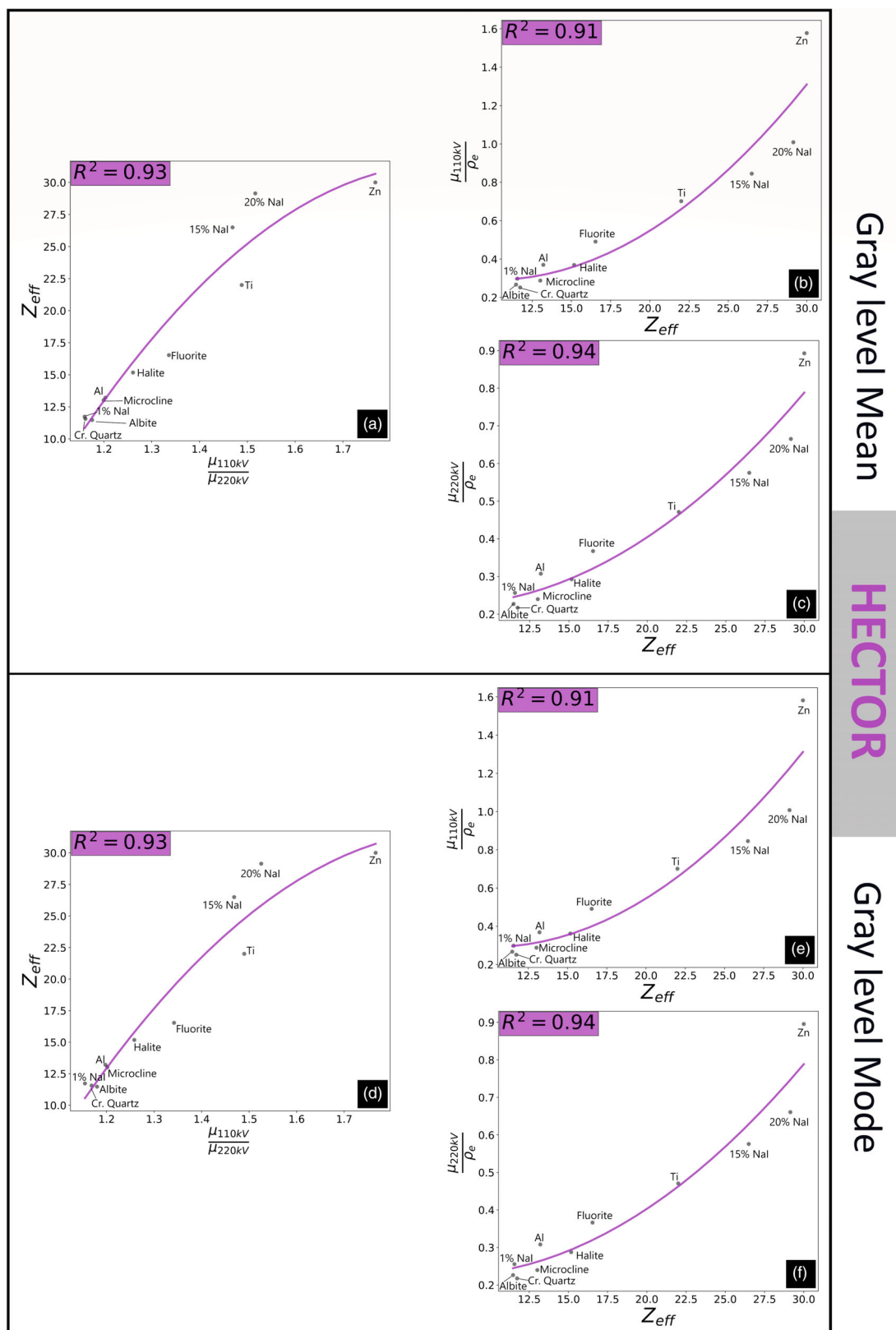


Figure 5. Calibration curves determined with HECTOR scanner and *m*-set of calibration samples. Using the mean of grey level histogram, there is (a) Z_{eff} model; (b) ρ_e model using $\mu_{110\text{ kV}}$; (c) ρ_e model using $\mu_{220\text{ kV}}$. Using the mode of grey level histogram, there is (d) Z_{eff} model; (e) ρ_e model using $\mu_{110\text{ kV}}$; (f) ρ_e model using $\mu_{220\text{ kV}}$.

Table 7.
 $Z_{eff, Meas}$ and $\rho_{e, Meas}$ measured using DECT and the HECTOR scanner, and using both mean and mode of grey level histograms

	HECTOR			
	Chalk	Haematitic oolite	Chert	
$Z_{eff, Calc}$	14.67	18.81	11.75	
$\rho_{e, Calc}$	4.35E+23	7.70E+23	7.00E+23	
$Z_{eff, Meas}$	15.18	18.79	11.71	Grey level Mode
% difference	3.5%	0.05%	0.3%	
$\rho_{e, Meas}$ using $\mu_{110\text{ kV}}$	4.57E+23	7.71E+23	6.58E+23	
% difference	4.9%	0.05%	5.9%	
$\rho_{e, Meas}$ using $\mu_{220\text{ kV}}$	4.52E+23	7.72E+23	6.80E+23	
% difference	3.8%	0.3%	2.8%	
$Z_{eff, Meas}$	15.25	18.91	11.72	Grey level Mean
% difference	4%	0.5%	0.2%	
$\rho_{e, Meas}$ using $\mu_{110\text{ kV}}$	4.72E+23	7.96E+23	6.77E+23	
% difference	8.5%	3.4%	3.2%	
$\rho_{e, Meas}$ using $\mu_{220\text{ kV}}$	4.42E+23	7.49E+23	6.71E+23	
% difference	1.4%	2.7%	4.04%	

The percentage difference is with $Z_{eff, Calc}$ and $\rho_{e, Calc}$ of Table 4.
The electron density ρ_e values are in units of moles $e^- \text{ cm}^{-3}$.

pronounced in the calibration obtained with HECTOR (Figure 5), and in this case correlation coefficients are slightly lower (i.e., 0.91 to 0.94). Both Arion and HECTOR Z_{eff} calibration curves (Figure 4a and Figure 5a and d) showed a concave shape, less pronounced for the former and more pronounced for the latter.

The rock characterisation based on effective atomic number and electron density obtained with μ values from Setup Optimizer have a maximum percent difference between simulated and calculated properties of 25% (specifically, for the haematitic oolite sample), which is comparable to that obtained with the medical CT scanner. However, the characterisation with HECTOR entails a bias between measured and calculated properties smaller than the modelled ones (Table 7), i.e., generally less than 5%. The explanation probably lies in the irregular sample shape. Set-up Optimizer considers mainly homogeneous cylindrical shape; thus, the simulation result may not be perfectly representative of the shape of the samples analysed here. A lower uncertainty could be reached by using cylindrical samples with the same diameter (in this study dimensions are comparable but not identical). Moreover, samples of irregular rather than round shape are most affected by beam hardening artefacts, which hamper image quality (Brunelle *et al.* 2016).

Although the general difference between the values obtained by the mean and the mode of grey levels is not significant, again the choice of the mode rather than mean in haematitic oolite characterisation improved the results. The

μ distribution histogram from a HECTOR slice is bimodal (Figure 10). It is quite different from the one reported in Figure 9, but the dissimilarity can easily be explained by the image resolutions, 600 μm for medical CT and 25 μm for HECTOR, which allows the latter to better discriminate between the two main components of this rock.

Table 7 shows that the bias with $Z_{eff, Calc}$ and $\rho_{e, Calc}$ is the smallest, entailing the best results among these three scanners. However, using grey level mode and μ calculated at high energy, 220 kV, is the best choice to determine ρ_e .

CoreTOM

The calibration curves obtained with the CoreTOM scanner using the same acquisition conditions as HECTOR and the same set of calibration materials (*m*-set) (Figure 6) yielded high correlation coefficients (R^2 between 0.88 and 0.97). An outlier (15% NaI) and a mismatch between data points and curves are visible in both Z_{eff} models (Figure 6a and d). The outlier is difficult to explain because other solutions perform well; moreover, this 15% NaI sample, despite not perfectly fitting the curve is not an outlier in the HECTOR calibration. Here, the Z_{eff} curve, unlike the one obtained with HECTOR, has a convex shape. This rock characterisation (Table 8) does not perform as well as those accomplished using HECTOR (Table 7), even though the acquisition settings were the same.

The calibration curves covering a wider range of energies (Figure 7) have lower correlation coefficients than those obtained using the same acquisition condition as HECTOR (Figure 6). As in the case of the medical CT scanner, using the mean rather than the mode of the histogram grey values did not provide an overwhelmingly lower percentage difference.

The $\mu_{90\text{ kV}} / \mu_{160\text{ kV}}$ settings of the CoreTOM are the closest to the medical CT scanner (i.e., 70/140 kV). It is interesting to note that the difference between calculated and measured properties is more pronounced when using the CoreTOM (a mean difference of about 7% for medical CT vs. a mean difference of about 12% for both Z_{eff} and ρ_e with CoreTOM). This is probably due to the differences in the detectors' technology with dissimilar sensitivities and to the use of two different kinds of filter for the incident X-ray beam; indeed, the bowtie filter for medical CT makes the X-ray bandwidth narrower than metal plates typically used in micro-CT (Primak *et al.* 2010).

Although the results presented in Table 9 show high variability, it is observed that $\mu_{160\text{ kV}} / \mu_{230\text{ kV}}$ allowed a

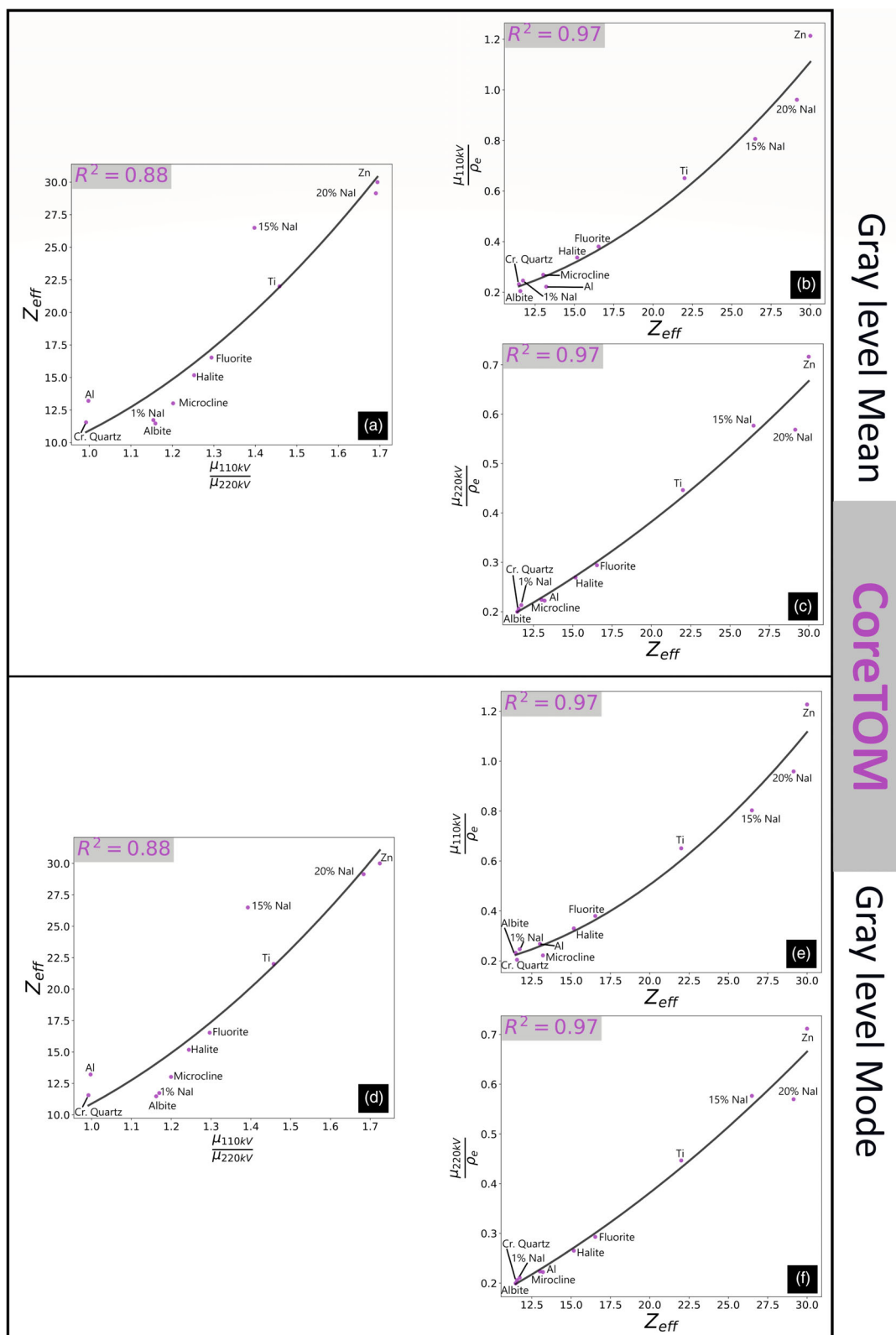


Figure 6. CoreTOM calibration curves for the CoreTOM scanner using the same acquisition conditions and set of calibration materials (*m*-set) of HECTOR. (a) Z_{eff} model; (b) ρ_e model using μ_{110} kV; (c) ρ_e model using μ_{220} kV using the mean of grey level histograms. (d) Z_{eff} model; (e) ρ_e model using μ_{110} kV; (f) ρ_e model using μ_{220} kV using the mode of grey level histograms.

Table 8.
 $Z_{eff, Meas}$ and $\rho_{e, Meas}$ measured using the CoreTOM scanner and the same DECT protocol previously used for the HECTOR scanner, and using both the mean and mode of grey level histograms

	CoreTOM			
	Chalk	Haematitic oolite	Chert	
$Z_{eff, Calc}$	14.67	18.81	11.75	
$\rho_{e, Calc}$	4.35E+23	7.70E+23	7.00E+23	
$Z_{eff, Meas}$	15.41	16.07	13.81	Grey level Mode
% difference	5%	14.5%	17.6%	
$\rho_{e, Meas}$ using $\mu_{110\text{ kV}}$	5.52E+23	1.05E+24	6.79E+23	
% difference	3.8%	36.7%	2.9%	
$\rho_{e, Meas}$ using $\mu_{220\text{ kV}}$	4.21E+23	9.71E+23	6.53E+23	
% difference	3.4%	26.03%	6.6%	
$Z_{eff, Meas}$	15.41	20.33	13.78	Grey level Mean
% difference	5.1%	8.2%	17.4%	
$\rho_{e, Meas}$ using $\mu_{110\text{ kV}}$	4.63E+23	9.45E+23	6.83E+23	
% difference	6.4%	22.7%	2.3%	
$\rho_{e, Meas}$ using $\mu_{220\text{ kV}}$	4.32E+23	8.61E+23	6.57E+23	
% difference	0.7%	11.8%	6%	

The percentage difference is with $Z_{eff, Calc}$ and $\rho_{e, Calc}$ of Table 4.
The electron density ρ_e values are in units of moles $e^- \text{ cm}^{-3}$.

lower percentage difference with calculated values, and this was observed to happen whenever the curve of the Z_{eff} model had a concave shape. In summary, the parameters that best characterise the three rocks using the CoreTOM scanner are: $\mu_{160\text{ kV}}/\mu_{230\text{ kV}}$ for Z_{eff} characterisation, $\mu_{160\text{ kV}}$ for ρ_e characterisation, use of the grey level histogram mode, with the g-set of calibration materials (Table 1).

Curve shape in Z_{eff} calibration model

The most important interaction between photons and materials in dual-energy CT techniques are photoelectric absorption and Compton scattering. As illustrated in Figure 11, the former dominates at lower energies and depends on target chemical composition (Z_{eff}), while the latter is predominant at higher energies and is more related to sample density (ρ_e) (Saldana-Gonzalez *et al.* 2012). It is not possible to determine a precise threshold energy between these two phenomena because it depends of the target composition and X-ray spectrum, which are specific to each X-ray tube of CT scanners (Johnson 2012).

Most geological materials have a high X-ray attenuation, so the energy used must be high enough to penetrate the material but not too high so as not to lose the influence of photoelectric absorption. Observing the graph in Figure 11, the best energy should be as close as possible to the

phenomena intersection to maximise the influence of photoelectric absorption and achieve good material penetration. Figure 12 shows an example of the attenuation coefficient and the interaction predominance according to different energies.

Observing the Z_{eff} model in Figure 7, the curve shape changes with increasing energy and it occurs in each calibration (Figures S1A and S1B show the curves achieved using every set of calibration materials). The plot obtained by $\mu_{90\text{ kV}}/\mu_{160\text{ kV}}$ (Figure 7a) has a convex fit, like the one obtained by the medical CT scanner (Figure 3), where the energies involved are comparable (70 kV and 140 kV). Increasing the high energy of the μ ratio ($\mu_{90\text{ kV}}/\mu_{230\text{ kV}}$) (Figure 7b) straightens the curve and increasing both energies further ($\mu_{160\text{ kV}}/\mu_{230\text{ kV}}$), makes the curve concave (Figure 7c). The 5% NaI solution is an outlier in Figure 7a, c; however, it does not exhibit the same behaviour in other calibration curves, and other solutes present in the calibration sets perform well. If these outliers were removed, the curve would remain concave (although less pronounced). Thus, the presence of this outlier seems not to change the concave/convex nature of the curve shape of the calibration models. The 160/230 kV couple of energies involved here is the most similar with those used in HECTOR (110 kV and 220 kV), where the Z_{eff} model also presents a concave shape (Figure 5).

Observing the results, the best estimation of the chemical composition of the rocks (by Z_{eff} and ρ_e) occurs at higher energies and when the shape of the Z_{eff} calibration curve becomes concave. The change from convex to concave of the Z_{eff} curve could be interpreted as revealing the shift from a photoelectric absorption dominated state to a Compton scattering dominated state.

Finding the best energy couple for each material based on the specific attenuation can be mathematically done if spectrum information is available. However, few laboratories have the necessary resources to calculate and measure the incident X-ray spectrum, and yet it is feasible to calculate the best acquisition settings as was done in this study with *Arion*. Thus, examining the curve shape in the calibration step could be a quick alternative to guide the choice of the best settings for material characterisation using stoichiometric DECT.

Scanner comparison

The three CT scanners characterised three different rocks with different levels of accuracy. The least effective scanner

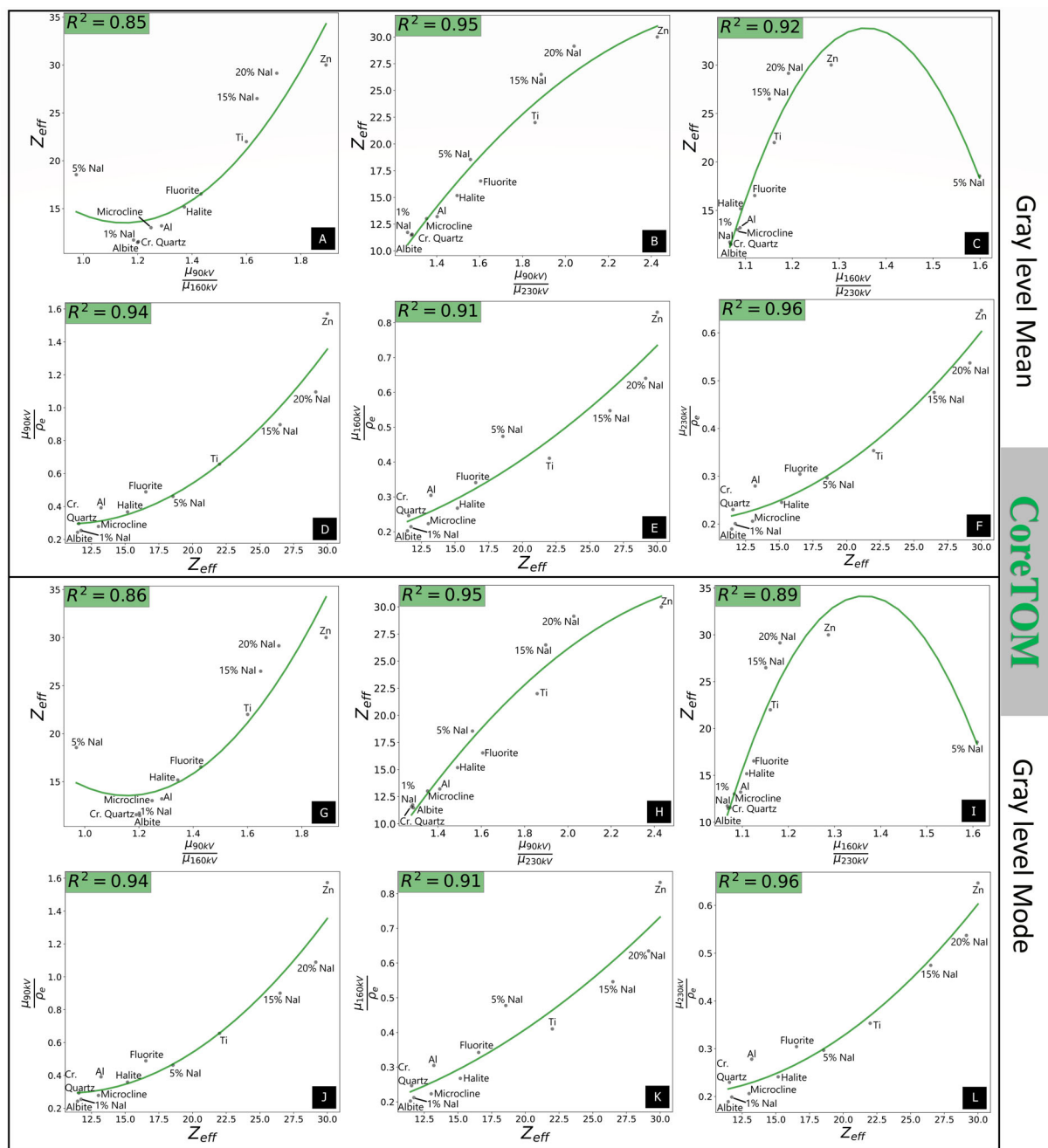


Figure 7. CoreTOM calibration curves. Z_{eff} calibration curves obtained using mean grey level histogram and μ_{90} kV/ μ_{160} kV (a), μ_{90} kV/ μ_{230} kV (b), and μ_{160} kV/ μ_{230} kV (c); using mode grey level histogram and μ_{90} kV/ μ_{160} kV (g), μ_{90} kV/ μ_{230} kV (h), and μ_{160} kV/ μ_{230} kV (i); ρ_e model obtained using mean grey level histogram and μ_{90} kV (d), μ_{160} kV (e), and μ_{230} kV (f); using mode grey level histogram and μ_{90} kV (j), μ_{160} kV (k), and μ_{230} kV (l).

was the medical CT, which led to measured $Z_{eff, Meas}$ and $\rho_{e, Meas}$ having up to a 10% bias on average compared with calculated values. This is not surprising because the medical CT and the image reconstruction algorithms are optimised to scan human bodies as quickly as possible, with the lowest possible doses and normalising the outcomes for air and water attenuation. They are not designed for

geological materials, and, as reported by Van Geet *et al.* (2000), they can be used before the micro-CT in a scaling-down approach. However, medical-CT can quickly scan large samples, and this is an advantage, especially when studying long geological core sequences for example. The CoreTOM performs better (the bias between the measured values and the expected values is approximately

Table 9.

Z_{eff_Meas} and ρ_{e_Meas} measured using DECT with three different energy couples, both mean and mode of grey level histograms and the CoreTOM scanner

Energy couple		CoreTOM			
		Chalk	Haematitic oolite	Chert	
	Z_{eff_Calc}	14.67	18.81	11.75	
	ρ_{e_Calc}	4.35E+23	7.70E+23	7.00E+23	
$\mu_{90\text{ kV}}/\mu_{160\text{ kV}}$	Z_{eff_Meas}	14.71	19.06	13.75	Grey level Mode
	% difference	0.3%	1.4%	17.1%	
	ρ_{e_Meas} using $\mu_{90\text{ kV}}$	5.01E+23	9.26E+23	6.48E+23	
	% difference	15.1%	20.2%	7.4%	
$\mu_{90\text{ kV}}/\mu_{230\text{ kV}}$	Z_{eff_Meas}	15.45	21.66	11.86	
	% difference	5.3%	15.2%	1%	
	ρ_{e_Meas} using $\mu_{90\text{ kV}}$	5.50E+23	9.78E+23	8.61E+23	
	% difference	26.2%	26.9%	23.1%	
$\mu_{160\text{ kV}}/\mu_{230\text{ kV}}$	Z_{eff_Meas}	14.86	19.95	11.24	
	% difference	1.3%	6.1%	4.3%	
	ρ_{e_Meas} using $\mu_{160\text{ kV}}$	4.55E+23	7.67E+23	7.10E+23	
	% difference	4.6%	0.4%	1.4%	
$\mu_{90\text{ kV}}/\mu_{160\text{ kV}}$	Z_{eff_Meas}	14.62	22.42	13.76	Grey level Mean
	% difference	0.3%	19.2%	17.1%	
	ρ_{e_Meas} using $\mu_{90\text{ kV}}$	4.75E+23	7.62E+23	6.13E+23	
	% difference	9.1%	1.2%	12.5%	
$\mu_{90\text{ kV}}/\mu_{230\text{ kV}}$	Z_{eff_Meas}	15.39	24.74	11.96	
	% difference	4.9%	31.6%	1.8%	
	ρ_{e_Meas} using $\mu_{90\text{ kV}}$	5.66E+23	1.03E+24	8.70E+23	
	% difference	30.1%	33.2%	24.3%	
$\mu_{160\text{ kV}}/\mu_{230\text{ kV}}$	Z_{eff_Meas}	15.94	24.32	11.74	
	% difference	8.6%	29.4%	0.02%	
	ρ_{e_Meas} using $\mu_{160\text{ kV}}$	4.33E+23	6.52E+23	6.98E+23	
	% difference	0.5%	15.4%	0.3%	
$\mu_{90\text{ kV}}/\mu_{230\text{ kV}}$	Z_{eff_Meas}	14.71	19.06	13.75	
	% difference	0.3%	1.4%	17.1%	
	ρ_{e_Meas} using $\mu_{90\text{ kV}}$	5.01E+23	9.26E+23	6.48E+23	
	% difference	15.1%	20.2%	7.4%	
$\mu_{160\text{ kV}}/\mu_{230\text{ kV}}$	Z_{eff_Meas}	15.45	21.66	11.86	
	% difference	5.3%	15.2%	1%	
	ρ_{e_Meas} using $\mu_{160\text{ kV}}$	5.50E+23	9.78E+23	8.61E+23	
	% difference	26.2%	26.9%	23.1%	

The percentage difference is with Z_{eff_Calc} and ρ_{e_Calc} of Table 4. The electron density ρ_e values are in units of moles $e^- \text{cm}^{-3}$.

5%, being the lowest bias) using higher energy. Although CoreTOM does not allow scanning large samples such as medical-CT (e.g., core about 2 m long and up to 65 cm in diameter (Martini *et al.* 2024)), it does allow analysis of cores up to one metre in length and with excellent measurement versatility (i.e., the source, sample holder and detector can move). HECTOR was the scanner that had the best characterisation results (less than 5% difference on average compared with calculated values). However, source and detector cannot move as CoreTOM does, limiting certain analyses. Moreover, HECTOR benefited from the simulation of the attenuation by Arion, optimising the choice of the best possible settings.

Another important difference among the three experiments is the resolution, related to a different scanning time (see section *Data acquisition*). Figure 13 shows the difference of the images captured with the haematitic oolite, the most heterogeneous specimen. On the left, the sample has been scanned with the medical CT at 140 kV and anisotropic voxels of $0.1 \times 0.1 \times 0.6 \text{ mm}$: its heterogeneity is barely visible. In the centre, the scan was obtained with CoreTOM at 160 kV and isotropic voxel size of $50 \mu\text{m}$: the resolution markedly improves, and the rock heterogeneity is clearly visible, although it is slightly noisy. On the right, the haematitic oolite has been scanned with HECTOR at 110 kV and an isotropic voxel size of $25 \mu\text{m}$, where details,

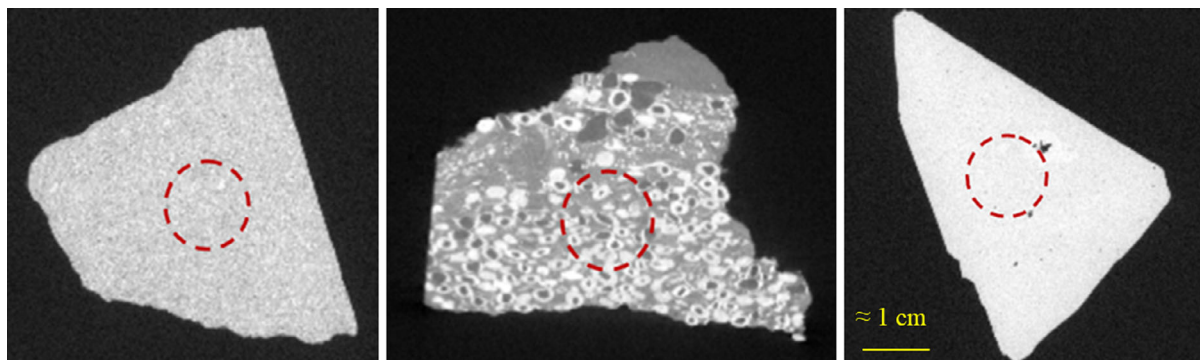


Figure 8. Slices of chalk (left), haematitic oolite (centre) and chert (right) acquired with the HECTOR scanner at 220 kV; the dotted circle indicates where analyses were performed.

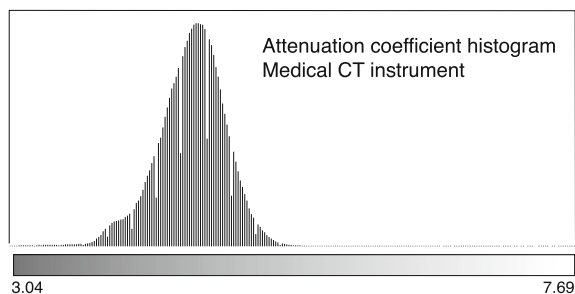


Figure 9. Grey level histogram of haematitic oolite acquired at 140 kV using the medical CT instrument.

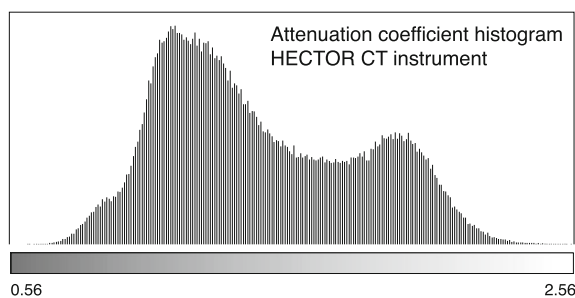


Figure 10. Grey level histogram of haematitic oolite acquired at 110 kV using the HECTOR scanner.

sharpness and contrast are excellent. The used reconstruction algorithms and software are different, yet influence the final result. Reconstruction parameters were optimised in each case to obtain the best possible image, except for the comparison between CoreTOM and HECTOR where the same filters, such as beam hardening correction and ring filter, were applied. A comparison of the influence of reconstruction algorithms on final results could further

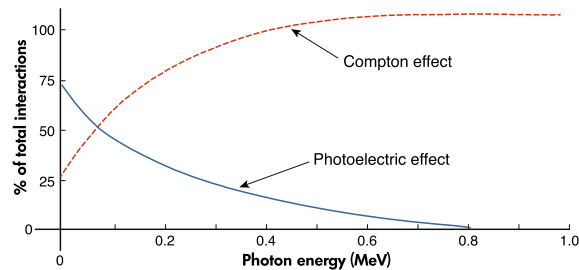


Figure 11. Rate of photoelectric absorption and Compton effect in relation to the incident beam energy. From Saldana-Gonzalez *et al.* (2012).

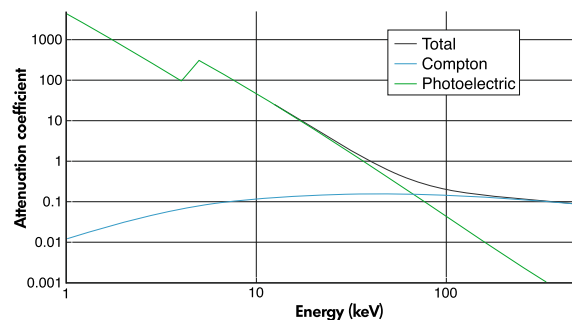


Figure 12. Attenuation coefficient of CaCO_3 for different photon energies and contributions of photoelectric effect (green) and Compton scattering (blue).

improve the understanding of characterisation studies, but is still under investigation.

A comparison of Figures 9 and 10 demonstrates that the resolution matters when analysing heterogeneous geological samples because the attenuation histograms can be quite different. This observation also outlines the

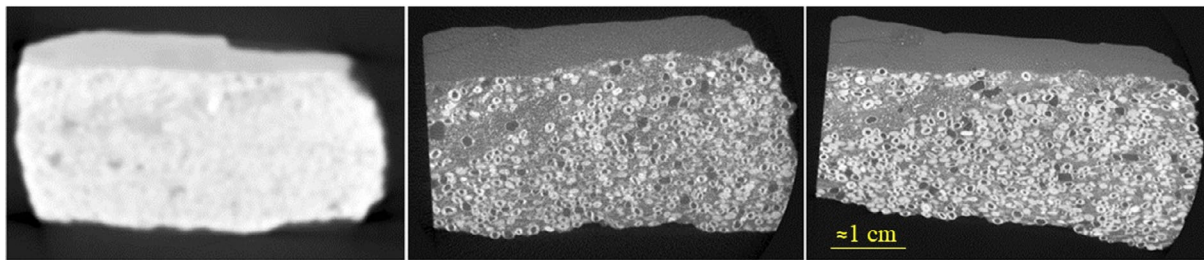


Figure 13. Haematitic oolite acquired with the three scanners. Slice scanned with medical CT and 600 μm resolution (left), CoreTOM and 50 μm resolution (centre), HECTOR and 25 μm resolution (right). The acquisition setting (see section *Data acquisition*) is similar for CoreTOM and HECTOR, while medical-CT differs by the very nature of the instrument.

need to use a $\mu\text{-CT}$ scanner to detect fine scale heterogeneities in a rock, for instance in the search for ore-bearing minerals.

Different sets of calibration materials (Table 1) were tested in this paper. Their choice played a fundamental role for the final characterisation according to the instrument. The *b*-set turned out to be best for the medical CT scanner, the *g*-set for the CoreTOM scanner and the *m*-set for the HECTOR scanner. Thus, it is not possible to define a universal set of calibration materials. The comparison between the calibration obtained with the HECTOR (Figure 5) and CoreTOM (Figure 6) scanners using identical settings confirms this observation: the attenuation of the samples, the correlation coefficients and the shape of the calibration curves change.

Conclusions

Three rocks (chalk, haematitic oolite and chert) with contrasting density, chemistry and mineralogy were analysed to precisely calculate their effective atomic number Z_{eff} and electron density ρ_e using chemical and mineralogical tests. This was compared with Z_{eff} and ρ_e values obtained by the dual-energy CT stoichiometric method using three different instruments: a medical CT scanner, a custom-built micro-CT device and a commercial micro-CT facility.

Five different energy couples, six sets of calibration materials, two statistical descriptors of grey level histograms to calculate μ and different resolutions were tested to study changes in the characterisation of the samples. The best setting of each scanner was evaluated using the lowest bias between the measured and the calculated Z_{eff} and ρ_e :

- about 10% difference using the medical CT scanner;
- less than 5% difference using HECTOR;
- about 5% difference using the commercial micro-CT.

Three rocks were also characterised with different levels of accuracy, having high, medium, and low relative bias compared with properties calculated with chemical and mineralogical data for medical CT, CoreTOM and HECTOR scanners, respectively. Yet, defining a general DECT protocol proved to be unfeasible because several factors must be considered: each scanner has its own instrumental properties that influence the measurement results, and, depending on the sample and the expected outcome, one instrument is more suitable than the other.

However, the following guidelines are proposed:

- the selection of the best statistical descriptor of the grey level histogram should consider the heterogeneity of rock samples to calculate the attenuation μ ;
- the best characterisations are obtained when the Z_{eff} calibration curve has a concave shape;
- the knowledge of the incident spectrum and a basic prior knowledge of the composition of the rock sample facilitates the selection of the best acquisition settings for a specific instrument, as shown by the results obtained with the HECTOR scanner. Yet, it does not turn out to be essential, as demonstrated by the results from the CoreTOM instrument.

In short, there are no universal best acquisition settings because they depend on the scanner characteristics, i.e., the incident spectrum and scanner geometry, and there is no perfect scanner because its choice depends on the type of samples being analysed and laboratory need.

The stoichiometric calibration method for dual-energy computed tomography (DECT) could be easily implemented in any laboratory equipped with a CT scanner to study geological samples. This paper suggests some hints to faster implement their laboratory protocol for a wide range of applications in Earth science studying a delimited region of interest. In the future, this measurement principle could be applied to the entire

sample to achieve a perfect match of quantitative and qualitative analysis in three dimensions. Moreover, the application of this method may be extended to different acquisition modalities, e.g., helical CT, to decrease cone-beam artefacts and improve the outcome precision.

Acknowledgements

This research was funded by *Fonds de recherche du Québec-Nature et technologies*, *Natural Sciences and Engineering Research Council of Canada*, *Canada Research Chairs Program* and *Canada Foundation for Innovation*. The *Excite Network* funded by the European Union's Horizon 2020 research and innovation programme under grant agreement No. 10100561 and the *UGent Core facility*, UGCT (BOF.COR.2022.0008). The authors thank Prof. Matthieu Boone (Ghent University), Dr. Jan Dewanckele (TESCAN), Philippe Letellier and Mathieu Des Roches (INRS) for their support and advice. The authors also thank Prof. Jean Carlos Serrano (Université du Québec à Rimouski) for conducting the XRD analyses.

Scientific editing by Thomas C. Meisel.

Data availability statement

Supplementary data and all sample scans accomplished with the different instruments are available at the *Borealis* repository: <https://doi.org/10.5683/SP3/UQ7GIJ>.

References

- Akbari A. (2015)**
Micro-CT scanning of soil aggregate: The importance of image thresholding. In: *2nd International Conference on Tomography of Materials and Structures (Québec, QB, Canada)*, 622–626.
- Alves H., Lima I., de Assis J.T., Neves A.A. and Lopes R.T. (2015)**
Mineralogy evaluation and segmentation using dual-energy microtomography. *X-Ray Spectrometry* 44, 99–104.
- Arnold J.R., Testa Jr. J.P., Friedman P.J. and Kambic G.X. (1983)**
Computed tomographic analysis of meteorite inclusions. *Science*, 219, 383–384.
- Azevedo S.G., Martz H.E., Aufderheide M.B., Brown W.D., Champley K.M., Kallman J.S., Roberson G.P., Schneberk D., Seetho I.M. and Smith J.A. (2016)**
System-independent characterization of materials using dual-energy computed tomography. *IEEE Transactions on Nuclear Science*, 63, 341–350.
- Baker D.R., Mancini L., Polacci M., Higgins M.D., Gualda G.A.R., Hill R.J. and Rivers M.L. (2012)**
An introduction to the application of X-ray microtomography to the three-600 dimensional study of igneous rocks. *Lithos*, 148, 262–276.
- Blunt M.J., Bijeljic B., Dong H., Gharbi O., Iglauer S., Mostaghimi P., Paluszny A. and Pentland C. (2013)**
Pore-scale imaging and modelling. *Advances in Water Resources* 51, 197–216.
- Boespflug X., Long B.F.N. and Occhietti S. (1995)**
Cat-scan in marine stratigraphy – A quantitative approach. *Marine Geology*, 122, 281–301.
- Bonnin A., Duvauchole P., Kafandjian V. and Ponard P. (2014)**
Concept of effective atomic number and effective mass density in dual-energy X-ray computed tomography. *Nuclear Instruments and Methods in Physics Research Section B*, 318, 223–231.
- Bourque A.E., Carrier J.F. and Bouchard H. (2014)**
A stoichiometric calibration method for dual energy computed tomography. *Physics in Medicine and Biology*, 59, 2059–2088.
- Brunelle C.B., Des Roches M., Daigle L-F., Francus P., Long B. and Després P. (2016)**
Combining CT scan and particle imaging techniques: Applications in geosciences. *The 4th International Conference on Image Formation in X-ray Computed Tomography*, 225–228.
- Bushberg J.T., Seibert J.A., Leidholdt E.M. and Boone J.M. (2012)**
The essential physics of medical imaging (third edition). Lippincott, Williams and Wilkins, (Philadelphia, PA, USA), 1048pp.
- Butler B.M. and Hillier S. (2021)**
powdR: An R package for quantitative mineralogy using full pattern summation of X-ray powder diffraction data. *Computers and Geosciences*, 147, 104662.
- Cnudde V. and Boone M.N. (2013)**
High-resolution X-ray computed tomography in geosciences: A review of the current technology and applications. *Earth-Science Reviews*, 123, 1–17.
- Cnudde V., Dewanckele J., Boone M., de Kock T., Boone M., Brabant L., Dusar M., de Ceukelaire M., de Clercq H., Hayen R. and Jacobs P. (2011)**
High-resolution X-ray CT for 3D petrography of ferruginous sandstone for an investigation of building stone decay. *Microscopy Research and Technique*, 74, 1006–1017.
- Cnudde V., Masschaele B., Dierick M., Vlassenbroeck J., Van Hoorebeke L. and Jacobs P. (2006)**
Recent progress in X-ray CT as a geosciences tool. *Applied Geochemistry*, 21, 826–832.
- Coenen J.C.G. and Maas J. (1994)**
Material classification by dual-energy computerized X-ray tomography. In: *International symposium on computerized tomography for industrial applications*, 120–127.

references

- Dewankele J., de Kock T., Boone M.A., Cnudde V., Brabant L., Boone M.N., Fronteau G., van Hoorebeke L. and Jacobs P. (2012)**
4D imaging and quantification of pore structure modifications inside natural building stones by means of high resolution X-ray CT. *Science of the Total Environment*, 416, 436–448.
- Dhaene J., Pauwels E., de Schryver T., De Muynck A., Dierick M. and Van Hoorebeke L. (2015)**
Arion: A realistic projection simulator for optimizing laboratory and industrial micro-CT. *Second International conference on tomography of materials and structures (Québec, Canada)*, 60–64.
- Di Schiavi Trotta L., Matenine D., Martini M., Stierstorfer K., Lemaréchal Y., Francus P. and Després P. (2022)**
Beam-hardening corrections through a polychromatic projection model integrated to an iterative reconstruction algorithm. *NDT and E International*, 126, 102594.
- Duliu O.G., Rizescu C.T. and Ricman C. (2003)**
Dual energy gamma-ray axial computer tomography investigation of some metamorphic and sedimentary rocks. *Neues Jahrbuch für Geologie und Paläontologie*, 228, 343–362.
- Eberl D.D. (2003)**
User guide to RockJock – A program for determining quantitative mineralogy from X-ray diffraction data. <https://doi.org/10.3133/ofr200378>.
- Fourie S. (1974)**
The cranial morphology of *Thrinaxodon liorhinus* Seeley. *Annals of the South African Museum*, 65, 337–400.
- Gagnon-Poiré A., Brigode P., Francus P., Fortin D., Lajeunesse P., Dorion H. and Trottier A-P. (2021)**
Reconstructing past hydrology of eastern Canadian boreal catchments using clastic varved sediments and hydro-climatic modelling: 160 years of fluvial inflows. *Climate of the Past* 17, 653–673.
- Godinho J.R.A., Westaway-Heaven G., Boone M.A. and Renno A.D. (2021)**
Spectral tomography for 3D element detection and mineral analysis. *Minerals*, 11, 598.
- Gordic S., Desbiolles L., Stolzmann P., Gantner L., Leschka S., Husarik D.B. and Alkadhi H. (2014)**
Advanced modelled iterative reconstruction for abdominal CT: Qualitative and quantitative evaluation. *Clinical Radiology*, 69, e497–504.
- Hendee W.R. (2002)**
Medical imaging physics (4th edition). Wiley-Liss (New York), 512pp.
- Iovea M., Oaie G., Ricman C., Mateiasi G., Neagu M., Szobotka S. and Duliu O.G. (2009)**
Dual-energy X-ray computer axial tomography and digital radiography investigation of cores and other objects of geological interest. *Engineering Geology*, 103, 119–126.
- Johnson T.R. (2012)**
Dual-energy CT: General principles. *American Journal of Roentgenology*, 199, (5 Suppl), S3–8.
- Kalender W. (2011)**
Computed tomography: Fundamentals, system technology, image quality, applications (third edition). Wiley-VCH (Weinheim), 372pp.
- Kastner J., Plank B. and Heinzl C. (2015)**
Advanced X-ray computed tomography methods: High resolution CT, quantitative CT, 4DCT and phase contrast CT. *Proceedings of the Digital Industrial Radiology and Computed Tomography Conference*. Gent BC Administratieve informatie (Gent, Belgium).
- Keller A.A. (1997)**
High resolution cat imaging of fractures in consolidated materials. *International Journal of Rock Mechanics and Mining Sciences*, 34, 155.e151–155.e116.
- Landry G., Seco J., Gaudreault M. and Verhagen F. (2013)**
Deriving effective atomic numbers from DECT based on a parameterization of the ratio of high and low linear attenuation coefficients. *Physics in Medicine and Biology*, 58, 6851–6866.
- Manohara S.R., Hanagodimath S.M., Thind K.S. and Gerward L. (2008)**
On the effective atomic number and electron density: A comprehensive set of formulas for all types of materials and energies above 1 keV. *Nuclear Instruments and Methods in Physics Research Section B*, 266, 3906–3912.
- Martini M., Francus P., Di Schiavi Trotta L., Letellier P., Des Roches M. and Després P. (2024)**
Exploring the application of dual-energy CT to discriminate sediment facies in a varved sequence. *The Depositional Record*, 10, 231–244.
- Martini M., Francus P., Di Schiavi Trotta L. and Després P. (2021)**
Identification of common minerals using stoichiometric calibration method for dual-energy CT. *Geochemistry, Geophysics, Geosystems*, 22, 1–14.
- Masschaele B., Dierick M., Van Loo D., Boone M.N., Brabant L., Pauwels E., Cnudde V. and Van Hoorebeke L. (2013)**
HECTOR: A 240 kV micro-CT setup optimized for research. *Journal of Physics: Conference Series*, 463, 012012.
- Mizutani R. and Suzuki Y. (2012)**
X-ray microtomography in biology. *Micron*, 43, 104–115.
- Ni X., Miao J., Lv R. and Lin X. (2017)**
Quantitative 3D spatial characterization and flow simulation of coal macropores based on μ CT technology. *Fuel*, 200, 199–207.



references

Pazireh M., Kingston A.M., Latham S.J., Fullagar W.K. and Myers G.M. (2016)

Tomography of atomic number and density of materials using dual-energy imaging and the Alvarez and Macovski attenuation model. *Journal of Applied Physics*, 119, 214901.

Primak A.N., Ramirez Giraldo J.C., Eusemann C.D., Schmidt B., Kantor B., Fletcher J.G. and McCollough C.H. (2010)

Dual-source dual-energy CT with additional tin filtration: Dose and image quality evaluation in phantoms and *in vivo*. *American Journal of Roentgenology*, 195, 1164–1174.

Re A., Corsi J., Demmelbauer M., Martini M., Mila G. and Ricci C. (2015)

X-ray tomography of a soil block: A useful tool for the restoration of archaeological finds. *Heritage Science*, 3, 4.

Remeysen K. and Swennen R. (2008)

Application of microfocus computed tomography in carbonate reservoir characterization: Possibilities and limitations. *Marine and Petroleum Geology*, 25, 486–499.

Saldana-Gonzalez G., Reyes U., Salazar H., Martinez O., Moreno E. and Conde R. (2012)

High density devices applied to a gamma-camera implementation. In: Ventzas D. (ed.), *Advanced Image Acquisition, Processing Techniques and Applications*, I. InTech 2012.

Spiers F.W. (1946)

Effective atomic number and energy absorption in tissues. *The British Journal of Radiology*, 19, 52–63.

Van Daele M., Cnudde V., Duycke P., Pino M., Urrutia R. and De Batist M. (2014)

Multidirectional, synchronously-triggered seismo-turbidites and debrites revealed by X-ray computed tomography (CT). *Sedimentology*, 61, 861–880.

Van den Bulcke J., Boone M.A., Dhaene J., Van Loo D., Van Hoorebeke L., Boone M.N., Wyffels F., Beeckman H., Van Acker J. and De Mil T. (2019)

Advanced X-ray CT scanning can boost tree ring research for Earth system sciences. *Annals of Botany*, 124, 837–847.

Van Geet M., Swennen R. and Wevers M. (2000)

Quantitative analysis of reservoir rocks by microfocus X-ray computerised tomography. *Sedimentary Geology*, 132, 25–36.

Vinegar H.J. and Wellington S.L. (1987)

Tomographic imaging of three-phase flow experiments. *Review of Scientific Instruments*, 58, 96–107.

Vlassenbroeck J., Masschaele B., Cnudde V., Dierick M., Pieters K., Van Hoorebeke L. and Jacobs P. (2006)

Octopus 8: A high performance tomographic reconstruction package for X-ray tube and synchrotron micro-CT. In: Desruets J., Viggiani G. and Bésuelle P. (eds), *Advances in X-ray tomography for geomaterials*. Wiley, 167–173.

Vlassenbroeck J., Dierick M., Masschaele B., Cnudde V., Van Hoorebeke L. and Jacobs P. (2006)

Software tools for quantification of X-ray microtomography at the UGCT. *Nuclear Instruments and Methods in Physics Research A*, 580, 442–445.

Watanabe Y. (1999)

Derivation of linear attenuation coefficients from CT numbers for low-energy photons. *Physics in Medicine and Biology*, 44, 2201–2211.

Zhao Y., Sun Y., Liu S., Chen Z. and Yuan L. (2018)

Pore structure characterization of coal by synchrotron radiation nano-CT. *Fuel*, 215, 102–110.

Supporting information

The following supporting information may be found in the online version of this article:

Figure S1A. Z_{eff} calibration curves obtained with the CoreTOM scanner at different energies and using different sets of calibration materials.

Figure S1B. ρ_e calibration curves obtained with the CoreTOM scanner at different energies and using different sets of calibration materials.

Table S1. Effective atomic number and electron density of calibration materials.

Table S2. Example of effective atomic number and electron density measured using linear attenuation coefficients μ from the Arion Optimizer and different sets of calibration materials.

Table S3. Results of the rocks' $Z_{eff, Meas}$ and $\rho_{e, Meas}$ measured using the DECT method with three different energy couples and the CoreTOM scanner.

This material is available from: <http://onlinelibrary.wiley.com/doi/10.1111/ggr.12608/abstract> (This link will take you to the article abstract).